Flexible control of terahertz chirality in twisted nematic liquid crystal cell with submillimeter thickness

Hui-Jun Zhao,[1] Fei Fan,[1,2] Song-Lin Jiang,[1] Xin-Hao Jiang,[1] Yun-Yun Ji,[1,*] and Sheng-Jiang Chang[1,2]

[1]*Institute of Modern Optics, Nankai University, Tianjin Key Laboratory of Micro-scale Optical Information Science and Technology, Tianjin 300350, China*

[2]*Tianjin Key Laboratory of Optoelectronic Sensor and Sensing Network Technology, Tianjin 300350, China*

(Received 29 March 2023; accepted 28 August 2023; published 21 September 2023)

Liquid crystal (LC), an anisotropic and tunable material, is widely used in phase shifters, polarization converters, and chiral devices. However, it is difficult for simple LC devices to achieve strong chiral response in the terahertz regime, even for cholesteric LCs. In this paper, we observe a strong optical rotation effect in a twisted nematic (TN) LC cell with submillimeter thickness; moreover, the magnetic field disturbance breaks the mirror symmetry of the whole structure and a discontinuous TN LC molecular alignment is formed, thus realizing the strong circular dichroism effect. The above two effects can also be actively tuned by electrically controlling the arrangement of LC molecules. First, without applying an external magnetic field, the dynamic modulation of the optical rotation angle in the above TN LC device can be as high as about 75°. Then, when a magnetic field in the *x*-axis direction is applied, the dynamic manipulation range of circular dichroism in the TN LC device can be up to 35 dB. Meanwhile, the dynamic polarization conversion function (from LP to CP or LP to LP) can also be achieved. The optical rotation and circular dichroism effect of this TN LC with submillimeter thickness offer a clear physical picture for the development of efficient and active terahertz polarization conversion and chiral devices.

DOI: 10.1103/PhysRevMaterials.7.095602

I. INTRODUCTION

The terahertz wave (THz) is an electromagnetic wave located in the frequency band range 10^{11}–10^{13} Hz. Due to its unique electromagnetic characteristics and spectral position, the THz wave has the advantages of frequency bandwidth, low photon energy, and high penetrability [1,2]. Flexible manipulation of THz wave polarization and chirality is of great significance for the new generation of 6G communication, high-resolution imaging, and chiral biological detection [3–5]. In general, structures that lack mirrored or inverted symmetry are called chiral objects, and they exhibit different optical responses to circularly polarized (CP) light with different spin states. Chiral effects can be quantitatively described by optical activity (OA) and circular dichroism (CD). OA represents the polarization rotation of linearly polarized (LP) light through chiral devices, that is, the phase difference of CP light under different spin states, and CD represents the difference in transmission of CP light in two different spin states passing through the chiral device [6–8]. However, because the wavelength of the THz wave is much longer than the general chiral molecular structure, there are few natural materials with strong chiral responses in the THz regime.

The development of artificial metadevices (such as metasurfaces, subwavelength gratings, photonic crystals, etc.) provides a new scheme for THz chirality and polarization control. The introduction of microstructure with geometric symmetry destruction leads to the asymmetric interaction between THz waves and substances, to flexibly control the chirality and polarization of THz waves [9–13]. For example, Singh *et al.* [9] proposed a planar metasurface composed of an array of coupled metal split-ring resonators; this metasurface lacks mirror symmetry and exhibits asymmetric THz radiation transmission in the 0.25–2.5-THz band. Cong *et al.* [10] report an electrically programmable synthetic chiral paradigm driven by a 10-V electrical bias with significant reconstructions between left-handed, right-handed, achiral, and racemic conformations. The outstanding feature of chiral metadevices is that their enhanced chiral response is orders of magnitude stronger than natural materials. However, the limitations of dispersion, bandwidth, and insertion loss are always present in these metadevices, and once most of the metadevices are manufactured, they are usually difficult to change except for mechanical deformation.

Liquid crystals (LCs) have significant uniaxial anisotropy in the THz regime; they can be flexibly manipulated by optical, electrical, or magnetic fields. They also possess the advantages of a simple preparation process, low cost, and easy active manipulation [14–18]. As a consequence, THz functional devices based on LCs have attracted great attention. On the one hand, separate LCs can be used for THz wave phase, polarization, and wavefront control [19–22]. For example, Song *et al.* [22] fabricated a two-dimensional LC polarization grating based on twisted LC using polarization holography. On the other hand, LC can also be integrated with artificial metasurface to realize dynamic control of the electromagnetic response through artificial design [23–27]. Liu *et al.* and Wu

*jiyunyun@nankai.edu.cn

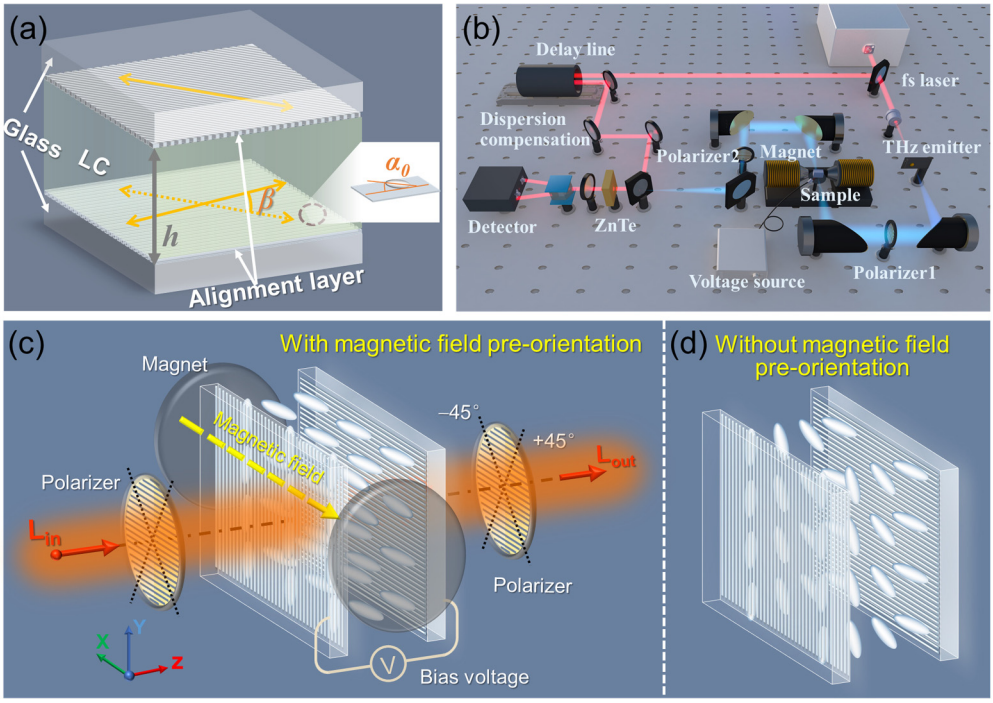

FIG. 1. (a) Schematic diagram of the structure of the LC device. (b) Schematic diagram of THz-TDPS. Diagram of the experimental setup of the LC device (c) with magnetic field pre-alignment and (d) without magnetic field pre-alignment.

et al. reported the programmable LC metasurface for THz beam steering [24,25]. However, no matter how the LC optical axis rotates, there is no optical chirality in a single anisotropic LC layer [26]. Twisted nematic (TN) LC cells can make LC devices in the visible regime display obvious chiral responses [28–30]. However, due to the long wave characteristics of THz waves and the limited birefringence coefficient of LCs, THz LC devices often need submillimeter thickness to achieve the required functions (such as sufficient phase delay, large optical rotation effect, etc.). There have been many studies on THz LC phase shift, but few on THz LC chiral control devices, especially for pure LC materials without metasurface. Zhang *et al.* [31] studied the THz chirality of cholesteric LCs at 250 K using the THz-TDS system. Nevertheless, the cholesteric LC has very weak chirality and limited tuning range in the THz regime at room temperature. To better design and develop efficient THz LC chiral control devices, it is necessary to clearly understand and study the chiral response of LC materials in the THz frequency range. Thus, THz chiral functional devices with simple processes and high efficiency can be further developed.

In this work, the tunable THz chiral effect in the TN LC cell with submillimeter thickness has been studied in the experiment. First, we observe a strong THz optical rotation effect in the TN LC cell when no external magnetic field is applied; Then, after the magnetic field is applied in the x direction, a discontinuous TN LC molecular alignment is formed owing to the disturbance of the magnetic field, which breaks the mirror symmetry of the whole structure thus realizing the strong circular dichroism and the polarization conversion effects. Besides, the above two effects can also be dynamically regulated by electrically controlling the arrangement of LC molecules.

II. METHODS

A. Device fabrication

The TN LC device in this work is prepared as the structure diagram shown in Fig. 1(a). First, two rubbed polyimide (PI) film-coated JGS1 glass substrates are used in a 500-μm-thick sandwich structure to homogeneously pre-anchoring LC molecules. JGS1 glass (High-purity UV optical quartz glass) is a high purity, high-temperature resistant and high light transmission quartz glass material. Second, a high birefringence nematic LC material (HTD028200) purchased by Jiangsu Hecheng Technology Co., Ltd. is filled into the above LC cell, which exhibits a positive dielectric anisotropy with a viscosity coefficient of 27 $mm^2\,s^{-1}$ (25 °C). Its transition temperatures from solid state to nematic state and from nematic state to isotropic state are $T_{SN} = -30$ °C and $T_{NI} = 103$ °C. Finally, the graphene dispersion solution is spin coated on the upper and lower glass substrates of the glued LC cell by rotating at 500 rpm for 1 min, and then dried at 80 °C to obtain a porous graphene conductive layer with a thickness of 500 nm. We spin a layer of graphene dispersion solution film on the upper and lower glass substrates of the glued LC cell.

In the absence of the external magnetic field and electric field, the TN LC molecules are arranged in the LC cell, as shown in Fig. 1(d). At this time, the twist angle of the LC molecules (i.e., the angle between the rubbing directions of the upper and lower glass substrates) is defined as β, and a pretilt angle of α_0 formed by the anchoring layer is used to avoid domain phase dislocation in LC devices. When a 70-mT constant magnetic field generated by a pair of rotatable permanent magnets on the x axis is applied to the LC cell, the original TN LC molecular arrangement will be destroyed,

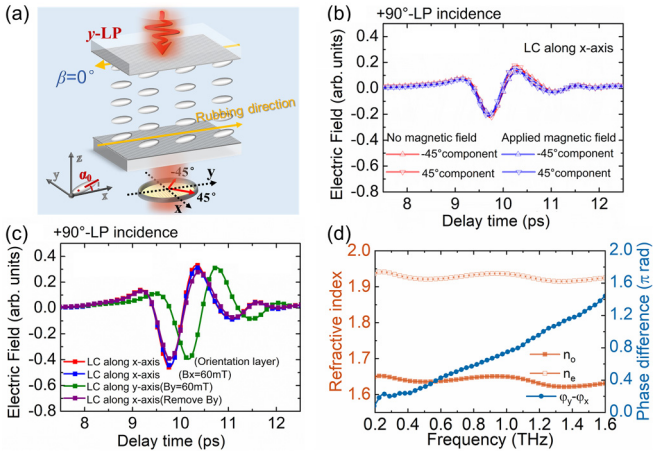

FIG. 2. For the case of $\beta = 0^\circ$. (a) Schematic diagram of CP light transmission in this situation; the experimental time-domain signals of $\pm 45^\circ$ orthogonal components (b) and y component (c) of output wave under y-LP incidence; (d) the normal refractive index n_o and extraordinary refractive index n_e of LC and its birefringence phase shift $\varphi_y - \varphi_x$.

and it will be approximately arranged along the magnetic field direction shown in Fig. 1(c). Next, an alternating electric field of 1 KHz with adjustable voltage is applied to control LC molecules in the TN LC cell, so that the direction of the LC optical axis can be controlled to rotate in space. We define the direction of the LC axis to rotate from the $x - y$ plane to the z axis at an angle of γ, and the angle between the LC axis and the x axis in the $x - y$ plane is α. The following work discusses the device performance caused by different geometric symmetries of LC devices under different LC molecular twist angles α and orientation angles γ.

B. Experimental system

The THz electromagnetic properties are characterized using a THz time-domain polarization spectroscopy (THz-TDPS) system, as shown in Fig. 1(b). THz pulses are generated by a GaAs photoconductive antenna, and a ⟨110⟩ ZnTe crystal for electro-optical sampling THz detection. The excitation source is a Ti:sapphire laser with an excitation source of 800 nm and a duration of 80 fs. All the experiments in this work were performed at room temperature ($20 \pm 5\,^\circ$C) and relative humidity <30%. The sample to be tested was placed at the focus of the system. Two permanent magnets placed on the left and right sides of the sample were used to generate a transverse magnetic field (x axis). Then an adjustable bias voltage was applied in the z direction to control the orientation of LC molecules. In addition, two THz metal wire polarizers were placed before and after the sample. The THz polarizer is a metal grating consisting of independent tungsten metal filaments with a pitch of 25 μm and a diameter of 10 μm, which has nearly 100% transmission and more than 99.8% degree of polarization in the THz frequency range discussed in this paper. Rotating the two polarizers to $\pm 45^\circ$ obtained the $\pm 45^\circ$ LP components under $\pm 45^\circ$ or -45° LP light illumination. Based on this, electromagnetic information including amplitude, phase, polarization, and chirality can be obtained from the Supplemental Material [32].

III. RESULTS AND DISCUSSION

A. Anchoring effect of the anchoring layer in LC devices

To characterize the anchoring effect of the anchoring layer, the rubbing direction of the upper and lower glass substrates are parallel (i.e., $\beta = 0^\circ$) and along the x axis [Fig. 2(a)]. In this case, a y-LP wave is experimentally incident into the device, and the output time-domain signals in different polarization directions are obtained by rotating the metal wire polarizer behind the sample. When no external magnetic field is applied, the LC molecule is completely oriented by the anchoring layer. By applying an external magnetic field of 60 mT, the orientation of the LC molecule is mainly affected by the magnetic field, because the alignment effect of the magnetic field is greater than that of the anchoring layer. First, the polarizer is set at $\pm 45^\circ$ to measure the $\pm 45^\circ$ orthogonal component of the output signals shown in Fig. 2(b). It can be seen that there is no time delay between the $\pm 45^\circ$ time-domain signal whether or not the x-axis magnetic field is applied, resulting in an LP output wave. This means that the LC molecules in this configuration are uniformly arranged along the magnetic field direction or anchoring direction. In other words, the anchoring layer possesses a good anchoring effect.

The recoverability of the above LC device is further characterized, and the experimental results are shown in Fig. 2(c). Here, the polarizer behind the sample is fixed on the y axis to detect the y-LP component of the output wave. First, as mentioned earlier, the alignment effect of the magnetic field applied in the x direction is the same as that of the anchoring layer, that is, the arrangement state of LC molecules does not change (along the x direction). At this time, the time domain signals in the above two cases are approximately coincident, as shown by the red dotted line and the blue dotted line in Fig. 2(c). Then, we turn the direction of the magnetic field to the y axis, and the orientation of the magnetic field will pull the LC molecules to the y direction. Therefore, the time domain signal has a certain delay, as shown by the green dotted line in Fig. 2(c). Finally, after removing the external magnetic field, the orientation effect of the anchoring layer will pull the LC molecule towards the x direction again, and the time domain signal will return to the original state, as shown by the purple dotted line in Fig. 2(c). In Fig. 2(d), the normal and extraordinary refractive indices (n_o and n_e) of the LC material can reach ∼1.95 and ∼1.65 in the frequency range 0.2–1.6 THz, whose birefringence coefficient (Δn) is about 0.3. Its ordinary and extraordinary absorption coefficients are shown in Fig. S1 in the Supplemental Material [32]. Moreover, the phase difference between the x polarization and the y polarization is obtained. At $f = 0.69$ THz, the maximum phase shift is $\pi/2$ rad. When $f = 1.22$THz, the maximum phase shift is π rad. These phenomena prove the anchoring effect of the anchoring layer on LC molecules and this anchoring effect is recoverable.

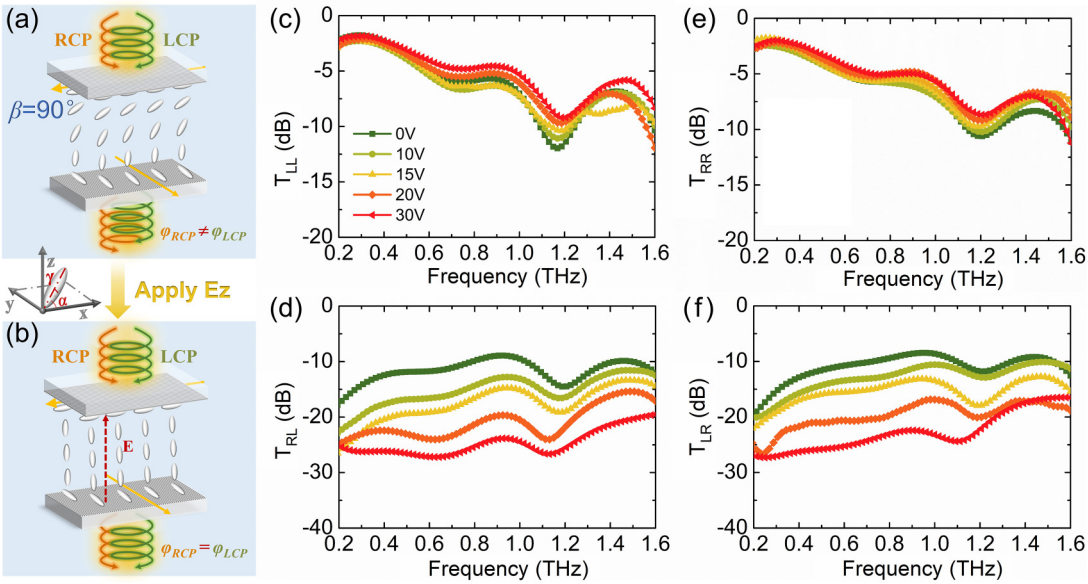

FIG. 3. For the case of $\beta = 90^\circ$ without magnetic field pre-alignment. Schematic diagram of CP wave transmission in TN LC cell without (a) and with (b) a biased voltage. The experimental CP power transmission spectra (c) T_{LL}, (d) T_{RL}, (e) T_{RR}, and (f) T_{LR} of the TN LC cell under the bias voltage of 0–30 V.

B. Tunable THz optical rotation effect in TN LC cell without magnetic field pre-alignment

Next, we discuss the optical rotation effect of the TN LC cell. Figures 3(a) and 3(b) show the CP power transmission diagram of a TN LC device without and with a biased electric field. In the absence of a biased electric field and with the rubbing direction of the upper and lower glass substrates orthogonal to each other (that is, the twist angle $\beta = 90^\circ$), the LC molecules in each tiny layer of the 500-μm-thick LC layer are uniformly arranged in different directions due to the two anchoring effects of the anchoring layer. Finally, the LC molecules between the upper and lower substrates rotate continuously by 90°. At this time, the two orthogonal CP lights produce a significant phase difference ($\varphi_{RCP} \neq \varphi_{LCP}$) without amplitude difference after passing through the TN LC layer in Fig. 3(a), exhibiting optical activity (i.e., pure optical rotation effect). Next, a bias voltage of 30 V is gradually applied to the TN LC cell along the z axis, so the LC molecules are gradually pulled towards the electric field as the bias voltage increases, which then eliminates the optical rotation effect of the incident wave ($\varphi_{RCP} = \varphi_{LCP}$), as shown in Fig. 3(b).

Subsequently, the power transmission spectra of four CP components, that is, two copolarized states (T_{LL} and T_{RR}) and two cross-polarized states (T_{RL} and T_{LR}), are obtained using the THz-TDPS system and then calculated using Eq. S(4) in the Supplemental Material [32]. When the bias voltage is 0 V, the output wave contains the co- and cross-polarized components for RCP or LCP incidence, as illustrated by the green dotted lines in Figs. 3(c)–3(f). Besides, the power transmission coefficients of the two polarized components (T_{RR} and T_{LR}) under RCP irradiation are approximately the same as that under LCP irradiation (T_{LL} and T_{RL}). The above phenomenon indicates that the TN LC device exhibits a pure optical rotation effect, rather than polarization conversion or circular dichroism. As the bias voltage increases, the power transmission coefficients of the two copolarized components increase slightly, while that of the two cross-polarized components decreases significantly. When the bias voltage increases to 30 V, the output wave only contains the copolarized component, with almost no optical rotation effect, as illustrated by the red dotted lines in Figs. 3(c)–3(f). Meanwhile, we conducted numerical simulations on a 500-μm-thick TN LC, and the details can be found in Sec. II of the Supplemental Material [32], and the simulated transmission spectra (Sec. III of Supplemental Material [32]) are consistent with the experimental results.

In addition, to reflect the optical chiral response of the device, two chiral parameters (i.e., CD and OA) need to be defined: copolarized circular dichroism (Co-CD) and copolarized optical activity (Co-OA), which are obtained from the two copolarized states and reflect the asymmetric transmission between the copolarized states (CD for power difference, OA for phase difference), as follows:

$$\text{Co-CD(dB)} = T_{LL} - T_{RR} = 20 \times \log_{10}(t_{ll}) - 20 \times \log_{10}(t_{rr}), \quad (1)$$

$$\text{Co-OA}(^\circ) = \tfrac{1}{2}(\varphi_{LL} - \varphi_{RR}), \quad (2)$$

where T_{LL} and T_{RR} are the power transmission (dB), and φ_{LL} and φ_{RR} represent the phase, respectively. The larger the absolute value of Co-CD, the closer the output wave is to a perfect CP state (a positive Co-CD represents a perfect LCP wave, and a negative one represents a perfect RCP wave). Figures 4(a) and 4(b) show the experimental Co-CD and Co-OA, which can be dynamically controlled by varying the bias voltage. At 0-V bias voltage, we observe a small CD (<10 dB) and a strong OA in the broadband range. Moreover, the value of OA increases in positive dispersion with the increase of THz frequency, and its maximum tuning range can reach 75°, as shown in Fig. 4(b). Both the CD and OA gradually decrease to 0 with the increase of the bias voltage. These

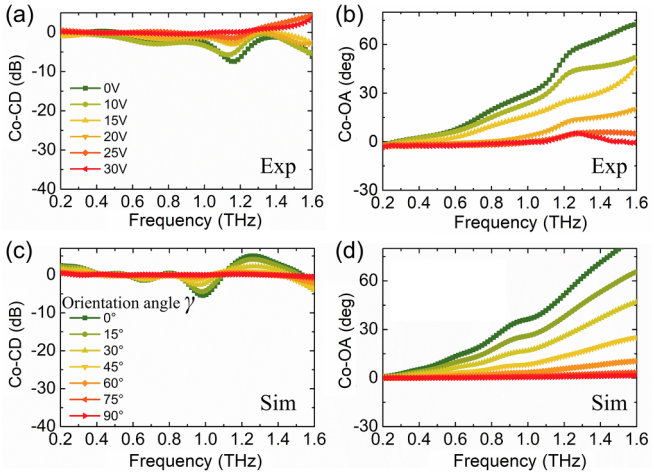

FIG. 4. For the case of $\beta = 90^\circ$ without magnetic field pre-alignment. The experimental Co-CD (a) and Co-OA (b) spectra of the TN LC cell with different bias voltages of 0–30 V. The simulated Co-CD (c) and (d) Co-OA spectra with different LC orientation angles of $\gamma = 0$–90°.

results demonstrate that the large optical rotation effect, weak circular dichroism effect, and its active tunable characteristic occur in the TN LC device. The simulated CD and OA spectra are obtained by using the finite-difference time-domain (FDTD) method in Figs. 4(c) and 4(d), which are similar to the experimental results. The bias voltage applied in the experiment can dynamically adjust the LC director. Therefore, in the simulation, we set different LC orientation angles to correspond to the experimental results. The larger the bias voltage, the larger the orientation angle.

As aforementioned, the propagation speed of LCP light is different from that of RCP light when passing through the TN LC device at 0-V bias voltage. At this time, if an LP wave is incident (which can be decomposed into two orthogonal CP waves), the output wave passing through the TN LC device will still be an LP wave with a certain polarization rotation angle (that is the pure optical rotation effect) as in Fig. 5(a). In Fig. 5(b), the optical rotation effect is eliminated when applying a 30-V bias electric voltage, resulting in an LP output wave with the same polarization direction as the incident wave. According to Eqs. S(5)–S(8) in the Supplemental Material [32], we calculate the four polarized components for LP incidence. The results suggest that the higher the THz frequency, the stronger the optical rotation effect of the TN LC device, as illustrated in Figs. 5(c)–5(f). As shown in Fig. S3 in the Supplemental Material [32], we also obtained the polarization ellipsoid angle (PEA) and polarization rotation angle (PRA) spectra according to Eqs. S(2) and S(3) in the Supplemental Material [32], and the results show that the maximum PRA can reach about 75° without a bias voltage when $f = 1.4$ THz. In addition, to describe the optical rotation effect of the device more intuitively, we further draw the polarization state of the output wave at a specific THz frequency ($f = 1.4$ THz) using Eq. S(1) in the Supplemental Material [32]. As the bias voltage increases from 0 to 30 V, the polarization direction of the output wave gradually rotates and finally pulls back to the polarization direction of the incident wave [Figs. 5(g) and 5(h)]. As can be seen, the optical rotation angle is about 75° for x-LP or y-LP incidence. These results demonstrate the tunable THz optical rotation effect of TN LC cells without magnetic field pre-alignment.

C. Tunable THz CD and polarization conversion of TN LC cell with magnetic field pre-alignment

First, we discuss the tunable CD effect of TN LC cells when an initial magnetic field of 60 mT is applied in the x direction. In this case, LC molecules that have been continuously twisted in the TN mode will be disturbed by the

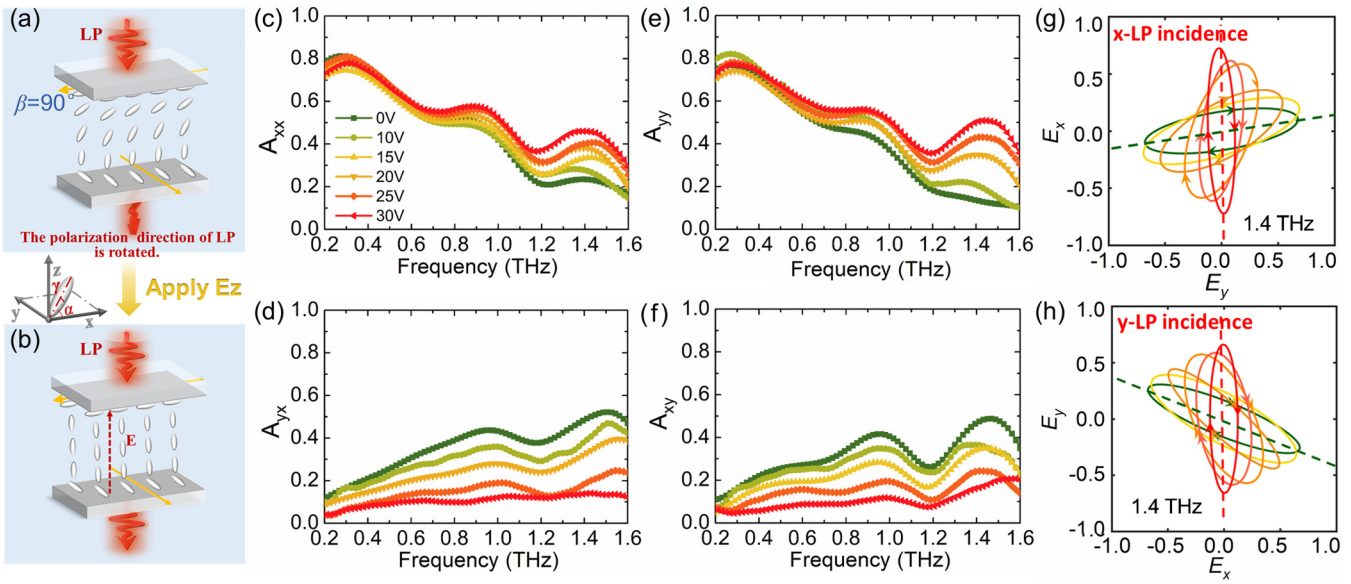

FIG. 5. For the case of $\beta = 90^\circ$ without magnetic field pre-alignment. Schematic diagram of LP wave transmission in TN LC cell without (a) and with (b) a biased voltage. The experimental LP amplitude transmission spectra (c) A_{xx}, (d) A_{yx}, (e) A_{yy}, and (f) A_{xy} of the TN LC cell under the bias voltage 0–30 V. The polarization ellipse at 1.4 THz for (g) x-LP incidence and (h) y-LP incidence.

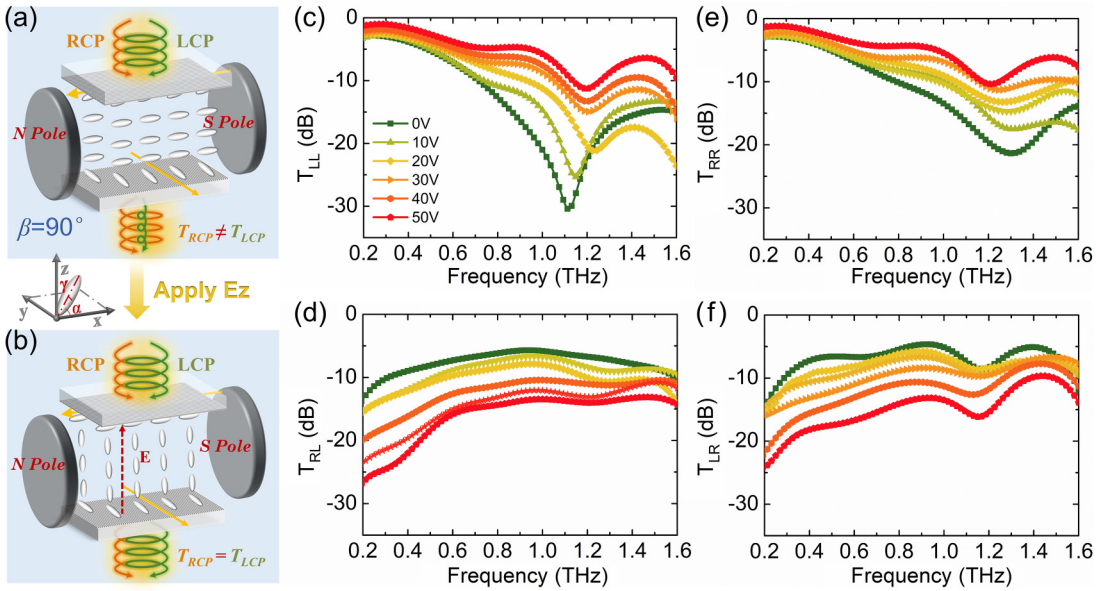

FIG. 6. For the case of $\beta = 90^\circ$ with magnetic field pre-alignment. Schematic diagram of CP wave transmission in TN LC cell without (a) and with (b) a biased electric field. The experimental CP power transmission spectra (c) T_{LL}, (d) T_{RL}, (e) T_{RR}, and (f) T_{LR} of the TN LC cell under the bias voltage 0–50 V.

external magnetic field, resulting in a discontinuous twisted LC molecule arrangement: the LC molecules far from the anchoring layer are uniformly arranged along the magnetic field direction (along the x axis), and the LC molecules closer to the upper and lower anchoring layers are gradually twisted to the rubbing direction due to strong anchoring effect. Thus, the twist angle of the LC molecules between the upper and lower anchoring layers is still 90°, and the LC molecules close to the substrate surface will produce a small pretilt angle. As a result, the mirror symmetry in the entire LC cell is seriously damaged, resulting in a strong CD response. The detailed geometric symmetry of the TN LC cell can be found in Sec. V of the Supplemental Material [32]. The two orthogonal CP lights produce significant power transmission differences ($T_{LCP} \neq T_{RCP}$), namely CD [Fig. 6(a)]. Next, by applying a bias voltage of 50 V to the TN LC cell along the z axis, the LC molecules are gradually pulled to the electric field direction as the bias voltage increases, as shown in Fig. 6(b), and the alignment effect of the longitudinal electric field greatly weakens the mirror symmetry breaking of the whole LC device, thus introducing almost no CD response ($T_{LCP} = T_{RCP}$).

Then, the power transmission spectra of four CP components are calculated, namely two copolarized states (T_{LL} and T_{RR}) and two cross-polarized states (T_{RL} and T_{LR}). When the bias voltage is 0 V, there is an obvious difference between the T_{LL} and T_{RR} states in power transmission spectra [the green lines in Figs. 6(c) and 6(e)], and a very small difference between the T_{RL} and T_{LR} states in power transmission spectra [the green lines in Figs. 6(d) and 6(f)]. With the increase of the bias voltage, the transmission of the two copolarized components gradually increases and the difference between them decreases, while the transmission of the two cross-polarized components gradually decreases, and the difference between them remains basically unchanged. When the bias voltage increases to 50 V, the differences between the T_{LL} and T_{RR} states and between the T_{RL} and T_{LR} states in power transmission spectra are almost 0 [the red lines in Figs. 6(d) and 6(f)]. That is to say, before and after applying the bias voltage, the transmission difference between cross-polarized components is always very small, which is an almost zero CD response of the cross-polarized states. Therefore, only the transmission and the difference between the two copolarized states are discussed below. As shown in Fig. S5 in the Supplemental Material [32], the simulated transmission spectra are consistent with the experimental results in this situation.

Figure 7 shows the power transmission difference (i.e., CD spectra) and phase difference (i.e., OA spectra) between the

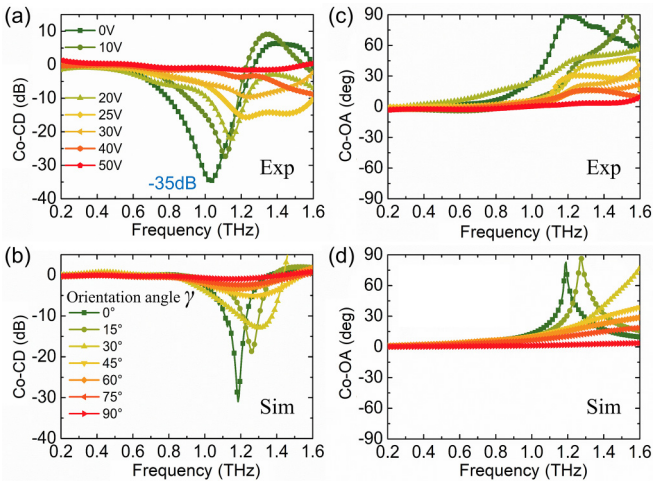

FIG. 7. For the case of $\beta = 90^\circ$ with magnetic field pre-alignment. The experimental Co-CD (a) and Co-OA (b) spectra of the TN LC cell with different bias voltages 0–50 V. The simulated Co-CD (c) and Co-OA (d) spectra with different LC orientation angles $\gamma = 0$–90°.

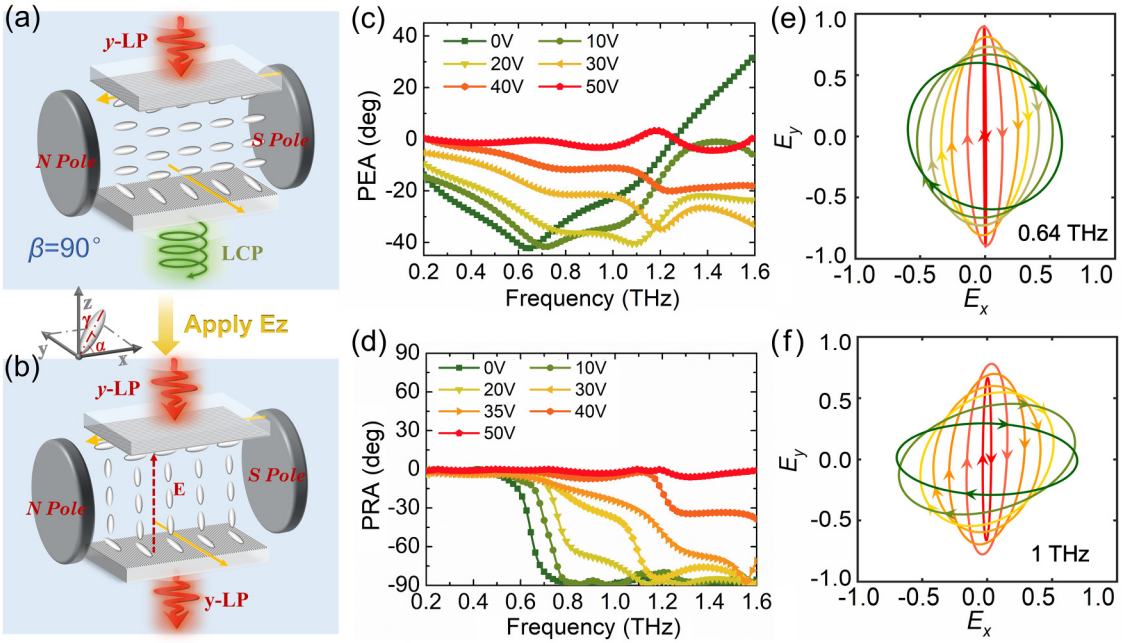

FIG. 8. For the case of $\beta = 90°$ with magnetic field pre-alignment. Schematic diagram of polarization conversion of LP light incident onto TN LC cell without (a) and with (b) a biased electric field. The PEA (c) and PRA (d) spectral with different bias voltages 0–50 V. The polarized ellipse of the output wave at 0.64 THz (e) and 1 THz (f).

two copolarized states. The experimental results in Figs. 7(a) and 7(b) indicate a strong CD and a strong OA in the broadband range of 0.6–1.6 THz without applying an external voltage. Here, a large CD of −35 dB can be achieved at 1.1 THz, and a large OA of 90° can be reached at 1.2 THz [the green lines in Figs. 7(a) and 7(b)]. With the increase of bias voltage, both CD and OA gradually decrease to 0 [the red lines in Figs. 7(a) and 7(b)]. These results mean that the TN LC device has a strong chiral effect (both CD and OA) when the external magnetic field is pre-aligned, and this chiral effect also possesses tunable characteristics. As can be seen, a tunable CD of −35 to 0 dB and a tunable OA of 90° to 0° are achieved over a wide spectral range. Furthermore, the simulated CD and OA spectra of the TN LC device using the FDTD simulation method can be obtained in Figs. 7(c) and 7(d), and the simulated results are consistent with the experimental results. Note that the chiral effect at this time is different from the pure optical rotation effect in Sec. III B, but is mainly a circular dichroism effect. We further experimentally detect the LP amplitude transmission spectra of the TN LC device when LP is incident on the device, and the results are shown in Fig. S6 in the Supplemental Material [32]. Both the results in the Supplemental Material and the above results in Sec. III C indicate that there is no optical rotation in the TN LC device at this time, but a strong circular dichroism effect.

To analyze the tunability of polarization conversion in the TN LC device, we fixed the polarization direction of the incident wave on the y axis, which is 45° with respect to the orientation angle of the LC molecules. In the absence of a biased electric field, the anisotropic LC layer can be regarded as a quarter wave plate, which makes a LP incident wave convert into a CP output wave after passing through the device (that is, the function of polarization conversion) [Fig. 8(a)]. With the increase of the bias voltage, the LC molecules are gradually pulled towards the direction of the electric field (i.e., the z axis), and the above polarization conversion effect gradually disappears, resulting in an output LP wave similar to the incident LP wave [Fig. 8(b)].

Then, the experimental PEA and PRA of the output wave are calculated accordingly in Figs. 8(c) and 8(d). Both PEA and PRA are dynamically regulated with the change of bias voltage. When the bias voltage is 0 V, PEA can reach 45° at 0.64 THz, and PRA can reach 90° in the broadband range 0.7–1.6 THz [the green lines in Figs. 8(c) and 8(d)]. With the increase of bias voltage to 50 V, the values of PEA and PRA gradually decrease to 0 [the red lines in Figs. 8(c) and 8(d)]. In this situation, the TN LC device not only has strong chiral effects (CD and OA) but also has polarization conversion effects due to the anisotropy of LCs. In addition, we further draw the polarization state of the output wave at specific THz frequencies. With the increase of the bias voltage, the output wave gradually changes from an approximate CP light to a perfect LP light with the polarization direction rotated about 43 ° at 0.64 THz [Fig. 8(e)]. When $f = 1.0$THz, the output wave gradually changes from an elliptically polarized state to an approximate CP state and then to an approximate LP state with the polarization direction rotated about 90° [Fig. 8(f)]. These experimental results agree with the above analysis of Fig. 8(a). In general, flexible manipulation of THz polarization conversion is achieved by controlling the arrangement of LC molecules with a variable electric field.

Finally, it is necessary to analyze THz chiral responses with different LC layer thicknesses for the case of $\beta = 90°$ with magnetic field pre-alignment. The Co-CD and Co-OA spectra of the TN LC cell are shown in Figs. 9(a) and 9(c). No matter how the thickness of the LC layer changes, the mirror symmetry of the TN LC device is always broken, so it has strong Co-CD and Co-OA in these cases. Moreover, the

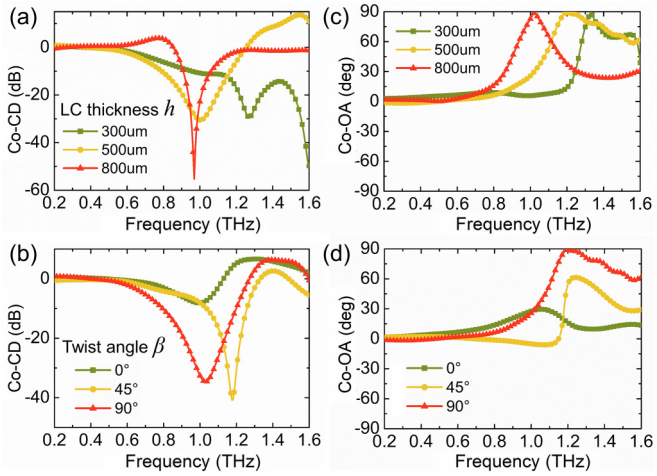

FIG. 9. The experimental Co-CD (a) and Co-OA (c) spectra with different LC thicknesses. The experimental Co-CD (b) and Co-OA (d) spectra with different twist angles β.

response frequency band of chirality (including Co-CD and Co-OA) gradually undergoes a redshift as the LC thickness increases, which is mainly due to the gradual redshift of the resonant position as the thickness of the sample increases, that is, the thickness of the intermediate LC layer. When the LC thickness is 500 μm, we analyze the THz chiral response of the TN LC cell with different twist angles. As shown in Figs. 9(b) and 9(d), the TN LC cell has different Co-CD and Co-OA as the twist angle β increases. When $\beta = 0^\circ$, the device still has a weak chirality (i.e., nonzero CD and OA), suggesting that there is still a weak mirror symmetry breaking in this LC cell. That is because the presence of pretilt angle α_0 causes LC molecules near the anchoring layer to not be well oriented by the magnetic field [the green lines in Figs. 9(b) and 9(d)]. Once the twist angle is not zero (e.g., $\beta = 45^\circ$ or 90°), the TN LC cell includes both weak mirror symmetry breaking caused by the pretilt angle and strong mirror symmetry breaking caused by the discontinuous twist of LC molecules. The two effects work together to produce a strong chiral response [the yellow and red lines in Figs. 9(b) and 9(d)].

IV. CONCLUSION

In summary, we fabricated a TN LC device with submillimeter thickness to dynamically control the THz chirality and polarization. In the absence of the magnetic field, a TN LC arrangement is formed when the twist angle $\beta = 90^\circ$ owing to the pre-anchoring effect of the anchoring layer, which produces a strong pure optical rotation effect. The dynamic modulation of optical activity (i.e., the optical rotation angle) is about 75° for the TN LC devices without applying an external magnetic field. Furthermore, after the x-axis magnetic field is applied, the magnetic field disturbance breaks the mirror symmetry of the whole structure, and a discontinuous TN LC molecular alignment is formed, thus realizing the strong circular dichroism effect. The dynamic regulation range of CD in this TN LC cell can be up to 35 dB. Meanwhile, the TN LC device can also realize the dynamic control of polarization conversion (from LP to CP or from LP to LP) under LP incidence. Our results pave the way to achieving feasible manipulation of THz polarization conversion and chiral response, which may inspire many future works (e.g., THz polarization imaging, chiral spectroscopy, and chiral sensing, etc.).

ACKNOWLEDGMENTS

This work was supported by the National Natural Science Foundation of China (Grants No. 61971242, No. 62205160, and No. 61831012), the National Key Research and Development Program of China (Grant No. 2017YFA0701000), and the Fundamental Research Funds for the Central Universities (Grant No. 63231159).

[1] R. Damari, O. Weinberg, D. Krotkov, N. Demina, K. Akulov, A. Golombek, T. Schwartz, and S. Fleischer, Strong coupling of collective intermolecular vibrations in organic materials at terahertz frequencies, Nat. Commun. **10**, 3248 (2019).

[2] K. Sengupta, T. Nagatsuma, and D. M. Mittleman, Terahertz integrated electronic and hybrid electronic-photonic systems, Nat. Electron. **1**, 622 (2018).

[3] Y. X. Wang, Y. Y. Yuan, G. H. Yang, X. M. Ding, Q. Wu, Y. N. Jiang, S. N. Burokur, and K. Zhang, Perfect Control of Diffraction Patterns with Phase-Gradient Metasurfaces, ACS Appl. Mater. Interfaces **14**, 16856 (2022).

[4] Y. Liu, H. Liu, M. Q. Tang, J. Q. Huang, W. Liu, J. Y. Dong, X. P. Chen, W. L. Fu, and Y. Zhang, The medical application of terahertz technology in non-invasive detection of cells and tissues: Opportunities and challenges, RSC Adv. **9**, 9354 (2019).

[5] W. J. Choi, G. Cheng, Z. Huang, S. Zhang, T. B. Norris, and N. A. Kotov, Terahertz circular dichroism spectroscopy of bio-materials enabled by kirigami polarization modulators, Nat. Mater. **18**, 820 (2019).

[6] M. A. Cole, W.-C. Chen, M. K. Liu, S. S. Kruk, W. J. Padilla, I. V. Shadrivov, and D. A. Powell, Strong Broadband Terahertz Optical Activity Through Control of the Blaschke Phase With Chiral Metasurfaces, Phys. Rev. Appl. **8**, 014019 (2017).

[7] M. Hentschel, M. Schaferling, X. Y. Duan, H. Giessen, and N. Liu, Chiral plasmonics, Sci. Adv. **3**, e1602735 (2017).

[8] V. S. Asadchy, C. Guo, I. A. Faniayeu, and S. Fan, Three-dimensional Random Dielectric Colloid Metamaterial with Giant Isotropic Optical Activity, Laser Photon. Rev. **14**, 2000151 (2020).

[9] R. Singh, E. Plum, C. Menzel, C. Rockstuhl, A. K. Azad, R. A. Cheville, F. Lederer, W. Zhang, and N. I. Zheludev, Terahertz metamaterial with asymmetric transmission, Phys. Rev. B **80**, 153104 (2009).

[10] L. Q. Cong, P. Pitchappa, N. Wang, and R. Singh, Electrically Programmable Terahertz Diatomic Metamolecules for Chiral Optical Control, Res. China **2019**, 7084251 (2019).

[11] C. Helgert, E. Pshenay-Severin, M. Falkner, C. Menzel, C. Rockstuhl, E. B. Kley, A. Tunnermann, F. Lederer, and T.

Pertsch, Chiral Metamaterial Composed of Three-Dimensional Plasmonic Nanostructures, Nano Lett. **11**, 4400 (2011).

[12] S. Zu, Y. J. Bao, and Z. Y. Fang, Planar plasmonic chiral nanostructure,s Nanoscale **8**, 3900 (2016).

[13] T. T. Kim, S. S. Oh, H. D. Kim, H. S. Park, O. Hess, B. Min, and S. Zhang, Electrical access to critical coupling of circularly polarized waves in graphene chiral metamaterials, Sci. Adv. **3**, e1701377 (2017).

[14] L. Wang, S. J. Ge, W. Hu, M. Nakajima, and Y. Q. Lu, Tunable reflective liquid crystal terahertz waveplates, Opt. Mater. Express **7**, 2023 (2017).

[15] R. Kowerdziej, K. Garbat, and M. Walczakowski, Nematic liquid crystal mixtures dedicated to thermally tunable terahertz devices, Liq. Cryst. **45**, 1040 (2018).

[16] B. Vasic, D. C. Zografopoulos, G. Isic, R. Beccherelli, and R. Gajic, Electrically tunable terahertz polarization converter based on overcoupled metal-isolator-metal metamaterials infiltrated with liquid crystals, Nanotechnology **28**, 124002 (2017).

[17] G. Isić, B. Vasić, D. C. Zografopoulos, R. Beccherelli, and R. Gajić, Electrically Tunable Critically Coupled Terahertz Metamaterial Absorber Based On Nematic Liquid Crystals, Phys. Rev. Appl. **3**, 064007 (2015).

[18] L. Wang, X. W. Lin, W. Hu, G. H. Shao, P. Chen, L. J. Liang, B. B. Jin, P. H. Wu, H. Qian, Y. N. Lu, X. Liang, Z. G. Zheng, and Y. Q. Lu, Broadband tunable liquid crystal terahertz waveplates driven with porous graphene electrodes, Light Sci. Appl. **4**, e253 (2015).

[19] C. F. Hsieh, C. S. Yang, F. C. Shih, R. P. Pan, and C. L. Pan, Liquid-crystal-based magnetically tunable terahertz achromatic quarter-wave plate, Opt. Express **27**, 9933 (2019).

[20] Y. Y. Ji, F. Fan, S. T. Xu, J. P. Yu, and S. J. Chang, Manipulation enhancement of terahertz liquid crystal phase shifter magnetically induced by ferromagnetic nanoparticles, Nanoscale **11**, 4933 (2019).

[21] A. K. Sahoo, C. S. Yang, O. Wada, and C. L. Pan, Twisted Nematic Liquid Crystal Based Terahertz Phase Shifter With Crossed Indium Tin Oxide Finger Type Electrodes, IEEE Trans. Terah. Sci. Technol. **9**, 399 (2019).

[22] S. Z. Li, Z. W. Zhao, C. M. Wang, Q. D. Wang, L. S. Yao, Z. H. Peng, Y. G. Liu, and L. Xuan, Electrically tunable photo-aligned two-dimensional liquid crystal polarisation grating, Liq. Cryst. **46**, 1175 (2019).

[23] H. J. Zhao, F. Fan, T. R. Zhang, Y. Y. Ji, and S. J. Chang, Dynamic terahertz anisotropy and chirality enhancement in liquid-crystal anisotropic dielectric metasurfaces, Photon. Res. **10**, 1097 (2022).

[24] C. X. Liu, F. Yang, X. J. Fu, J. W. Wu, L. Zhang, J. Yang, and T. J. Cui, Programmable Manipulations of Terahertz Beams by Transmissive Digital Coding Metasurfaces Based on Liquid Crystals, Adv. Opt. Mater. **9**, 2100932 (2021).

[25] J. B. Wu, Z. Shen, S. J. Ge, B. W. Chen, Z. X. Shen, T. F. Wang, C. H. Zhang, W. Hu, K. B. Fan, W. Padilla, Y. Q. Lu, B. B. Jin, J. Chen, and P. H. Wu, Liquid crystal programmable metasurface for terahertz beam steering, Appl. Phys. Lett. **116**, 131104 (2020).

[26] Y. Y. Ji, F. Fan, Z. Y. Zhang, Z. Y. Tan, X. Zhang, Y. W. Yuan, J. R. Cheng, and S. J. Chang, Active terahertz spin state and optical chirality in liquid crystal chiral metasurface, Phys. Rev. Mater. **5**, 085201 (2021).

[27] O. Buchnev, N. Podoliak, K. Kaltenecker, M. Walther, and V. A. Fedotov, Metasurface-based optical liquid crystal cell as an ultrathin spatial phase modulator for THz applications, ACS Photonics **7**, 3199 (2020).

[28] T. C. Lin, I. R. Nemitz, J. S. Pendery, C. P. J. Schubert, R. P. Lemieux, and C. Rosenblatt, Nematic twist cell: Strong chirality induced at the surfaces, Appl. Phys. Lett. **102**, 134101 (2013).

[29] K. Takatoh, M. Akimoto, H. Kaneko, K. Kawashima, and S. Kobayashi, Molecular arrangement for twisted nematic liquid crystal displays having liquid crystalline materials with opposite chiral structures (reverse twisted nematic liquid crystal displays), J Appl. Phys. **106**, 064514 (2009).

[30] L. Duda, M. Czajkowski, B. Potaniec, and P. Vankatova, Helical twisting power and compatibility in twisted nematic phase of new chiral liquid crystalline dopants with various liquid crystalline matrices, Liq. Cryst. **46**, 1769 (2019).

[31] X. Zhang, F. Fan, Y. Y. Ji, and S. J. Chang, Temperature-dependent chirality of cholesteric liquid crystal for terahertz waves, Opt. Lett. **45**, 4988 (2020).

[32] See Supplemental Material at http://link.aps.org/supplemental/10.1103/PhysRevMaterials.7.095602 for additional details regarding data processing, numerical simulation, absorption coefficient of the HTD028200 LC, the simulated CP power transmission spectra without magnetic field pre-alignment and with magnetic field pre-alignment, the polarization state in TN LC cell without magnetic field pre-anchoring and tunable transmission spectrum of LP wave transmission, and the mirror-asymmetry of the TN LC cell with magnetic field pre-alignment (Figs. S1–S6). S1: The ordinary and extraordinary absorption coefficient of the HTD028200 LC. S2: The simulated CP power transmission spectra of the TN LC cell under 0–90° LC orientation without magnetic field pre-alignment. S3: Experimental polarization conversion spectra without magnetic field pre-alignment. S4: The geometric symmetry of the TN LC cell with magnetic field pre-alignment. S5: The simulated CP power transmission spectra of the TN LC cell under 0–90° LC orientation with magnetic field pre-alignment. S6: The experimental LP transmission spectra with magnetic field pre-alignment. Supplemental Material includes additional Refs. [33–35].

[33] H. G. Berry, G. Gabrielse, and A. E. Livingston, Measurement of the Stokes parameters of light, Appl. Opt. **16**, 3200 (1977).

[34] C. Menzel, C. Rockstuhl, and F. Lederer, Advanced Jones calculus for the classification of periodic metamaterials, Phys. Rev. A **82**, 053811 (2010).

[35] Z. Wang, F. Cheng, T. Winsor, and Y. Liu, Optical chiral metamaterials: A review of the fundamentals, fabrication methods and applications, Nanotechnology **27**, 412001 (2016).